

Unusual Evolution of the Magnetic Interactions versus Structural Distortions in $RMnO_3$ Perovskites

J.-S. Zhou and J. B. Goodenough

Texas Materials Institute, 1 University Station, ETC 9.104, University of Texas at Austin, Austin, Texas 78712, USA

(Received 13 April 2006; published 19 June 2006)

We report the refinement of x-ray powder diffraction together with magnetic and thermal conductivity measurements made on the entire family of $RMnO_3$ perovskites prepared by melt growth or under high pressure. Analysis of the data has identified the origin of the transition from type-A to type-E magnetic order as a competition between t -orbital and e -orbital spin-spin interactions within each Mn-O-Mn bond in the (001) planes, the e -orbital interactions decreasing with decreasing R^{3+} -ion size.

DOI: 10.1103/PhysRevLett.96.247202

PACS numbers: 75.30.Et, 71.70.Ej, 72.15.Eb

From elastic-energy considerations, $LaMnO_3$ was initially proposed to undergo a cooperative orbital ordering below a T_{JT} that places the e electron of high-spin $Mn^{3+}:t^3e^1$ in the (001) plane [1]. The predicted orbital ordering and the consequent anisotropic magnetic couplings in $LaMnO_3$ were proven a few years ago by resonance x-ray scattering [2] and neutron inelastic scattering [3]. At $T > T_{JT}$, the Jahn-Teller (JT) distortion remains dynamic, as has been shown by x-ray absorption spectroscopy [4], and the vibronic states are degenerate in the (Q_2, Q_3) plane describing the E_g lattice-vibration breathing modes of a $MnO_{6/2}$ octahedron. Q_2 is orthorhombic and Q_3 is tetragonal. The introduction of anharmonic terms in the Hamiltonian changes the “Mexican hat” form of the potential in the (Q_2, Q_3) plane into three wells separated by $\theta_a = 120^\circ$ in the (Q_2, Q_3) plane for an isolated molecular complex. However, the cooperative JT distortion results in a two-well potential in the case of $LaMnO_3$ [5]. As pointed out by Kanamori [6], the cooperative JT distortion in orthorhombic $LaMnO_3$ does not have the two potential wells in exactly the directions of $\theta_a = 2\pi/3$ and $4\pi/3$ in the (Q_2, Q_3) plane as predicted from the classic 120° model, but they are leaning towards the $\pm Q_2$ axis. This shift is caused by a mixing of the JT distortion modes and an intrinsic octahedral-site distortion in the orthorhombic perovskite structure [7]. On the other hand, the overlap integral entering the perturbation formula $J \approx 4b^2/U$ of the superexchange spin-spin interaction depends on the $(180^\circ - \omega)$ Mn-O-Mn bond angle, which decreases monotonically as the ionic radius (IR) of rare-earth R^{3+} ion decreases. In comparison with the perovskite $RFeO_3$ family where Fe^{3+} is not JT active, the phase diagram of the $RMnO_3$ perovskites is more complex as is seen in Fig. 1. Although the perovskite $RMnO_3$ family shows a gradual structural change as IR decreases, the orbital ordering remaining the same as that in $LaMnO_3$ below T_{JT} , the phase diagram is divided sharply into three regions: (1) type-A spin order [ferromagnetic (001) planes coupled antiparallel] with a T_N that is extremely sensitive to IR, (2) a phase without classic spin ordering, and (3) type-E spin order [alternating ferromagnetic and antiferromag-

netic coupling in (001) planes] below an IR-independent T_N . How the JT and the intrinsic octahedral-site distortions influence the magnetic coupling and whether the evolution of the octahedral-site distortions and the Mn-O-Mn bond angle as a function of IR are sufficient to account for the complicated phase diagram of the $RMnO_3$ perovskites remain open questions for two reasons: (a) the existing phase diagram of the $RMnO_3$ perovskites does not cover the heavy rare earths since some members of group II $RMnO_3$ ($R = Y, Ho, Er, \dots, Lu$) need to be synthesized as perovskites under high pressure; and (b) for group I $RMnO_3$ ($R = La, \dots, Dy$), the available structural data

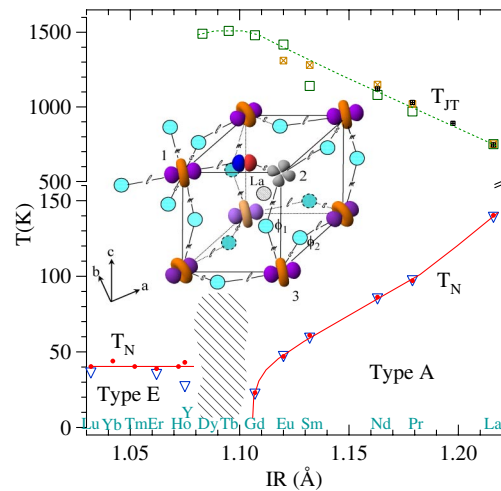


FIG. 1 (color online). Transition temperatures versus R^{3+} -ion radius (IR) in the perovskite $RMnO_3$ family. The T_N values shown by solid circles were obtained from magnetization measurements in a magnetic field of 20 Oe. Open triangles mark the temperature where the thermal conductivity $\kappa(T)$ shows an anomaly. The JT transition temperatures T_{JT} are taken from Refs. [8–10]. See the text for the meaning of the shaded area. Inset: Schematic drawing of the octahedral-site rotations and the e -orbital ordering in a primary unit cell of the cubic perovskite structure. The arrows point to axes for the unit cell of the orthorhombic $Pbnm$ structure. The unoccupied e orbital is placed at site 2 along with the occupied orbital in the other sites to illustrate the e^1 -O- e^0 coupling in the ab plane.

from neutron diffraction are incomplete due to strong neutron absorption in some rare earths such as $R = \text{Sm, Eu, Gd}$. In this Letter, we resolve these issues by refining the crystal structure from x-ray powder diffraction over the entire perovskite RMnO_3 family, including group II RMnO_3 perovskites synthesized recently under high pressure [11] and by supplying a complete phase diagram based on measurements of magnetization and thermal conductivity of the RMnO_3 perovskites. The structural data in this work and from previous neutron diffraction enable us to distinguish the factors contributing to the superexchange interactions and to identify the competition that is responsible for the evolution of magnetic phases in the RMnO_3 perovskites.

Single-crystal samples were grown with an infrared-heating image furnace under an atmosphere of Ar for $R = \text{La, ... , Eu}$ and air for $R = \text{Gd, Tb, Dy}$. The RMnO_3 perovskites with $R = \text{Y, Ho, ... , Lu}$ were synthesized under high pressure [11]. Powder x-ray diffraction (XRD) was carried out on pulverized crystals and ceramic samples in a Philips X'pert diffractometer with scan step $0.02^\circ/10 \text{ s}$. Structural parameters were obtained by fitting XRD data with the space group $Pbnm$ by the Rietveld method (FULLPROF program).

The average room-temperature ($180^\circ - \omega$) Mn-O-Mn bond angle $\langle \theta \rangle$ and three Mn-O bond lengths [the long and short Mn-O_{II} of the (001) and the c -axis Mn-O_I] are shown as a function of IR in Fig. 2. We have also superimposed on our x-ray data all neutron-diffraction data available to us. Although the Mn-O_{II} bond lengths of the high-pressure samples are a bit scattered due to relatively lower crystal-line quality and the scattering from heavy rare earths, our x-ray data are highly consistent with the available neutron-diffraction data for $R = \text{La, ... , Dy}$. More importantly, the x-ray diffraction data fill in the gap in the range of IR where it is difficult to perform neutron diffraction. This most complete data set allows us to extract more precisely the evolution with IR of the Q_2 and Q_3 modes. The lines in Fig. 2 are a guide to the eye, but fittings to these lines are used in the following discussion. The octahedral-site rotations due to a tolerance factor $t < 1$ reduce $\langle \theta \rangle$ as IR decreases. Curves of $\langle \theta \rangle$ versus IR and of the average bond length $\langle \text{Mn-O} \rangle$ versus IR are similar to those of the RFeO_3 perovskites. It is also commonly seen in both RMnO_3 and RFeO_3 families that the M-O_I and two M-O_{II} bond lengths are clearly separated into a medium, long, and short bond. The long and short Mn-O_{II} bonds undergo a broad maximum within $\text{IR} = 1.10\text{--}1.15 \text{ \AA}$, whereas the medium Mn-O_I bond length shows a minimum at nearly the same IR. These features originate from the intrinsic octahedral-site distortions since a similar bond-length splitting and its evolution against IR have also been found in RFeO_3 [7]. The cooperative JT distortion enhances significantly the magnitude of the bond-length splitting in the RMnO_3 .

The spin-spin coupling through $\text{Mn}^{3+}\text{-O-Mn}^{3+}$ bonds consists of the $t\text{-O-}t$ and $e\text{-O-}e$ superexchange interactions.

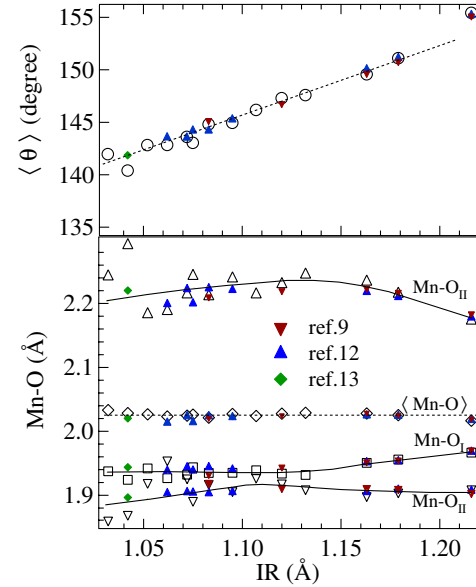


FIG. 2 (color online). The IR dependences of the average Mn-O-Mn bond angle $\langle \theta \rangle = 180^\circ - \omega$ and Mn-O bond lengths in the RMnO_3 perovskites. Data points marked by solid symbols are taken from neutron diffraction [9,12,13].

The anisotropic couplings of $e^0\text{-O-}e^0$ along the c axis and $e^1\text{-O-}e^0$ in the ab plane due to the cooperative orbital ordering are superimposed on the 3D antiferromagnetic $t^3\text{-O-}t^3$ interaction, which is seen in the type- G antiferromagnetic (AF) order of $\text{Ca}_{1-x}\text{Sr}_x\text{MnO}_3$ [14]. The measured [3] J_c and J_{ab} are the summation of exchange interactions from both t and e orbitals. Whereas the $t^3\text{-O-}t^3$ AF coupling is reinforced by the AF coupling from $e^0\text{-O-}e^0$ in the $\text{Mn-O}_I\text{-Mn}$ bonds along the c axis, the ferromagnetic (F) $e^1\text{-O-}e^0$ coupling dominates J_{ab} . Weakening of the F $e^1\text{-O-}e^0$ coupling leads to a competition between the AF $t^3\text{-O-}t^3$ interaction and the F $e^1\text{-O-}e^0$ interaction in the ab plane as IR decreases, which is the likely driving force behind the complex phase diagram of Fig. 1. A question to be clarified is whether weakening of the F coupling is due to either reduction of the Mn-O-Mn bond angle or changing of the octahedral-site distortions described by the Q_2 and Q_3 modes.

In order to answer the first question, we have made a plot in Fig. 3 of T_N and $\cos^2(\omega/2)$ versus IR since the $\langle \text{Mn-O} \rangle$ bond length d in the overlap integral [15] $b \approx \cos(\omega/2)/d^{3.5}$ is essentially independent of IR. Similar IR dependences of T_N and $\cos^2(\omega/2)$ in Fig. 3 for the type- A spin-ordered phase indicate that $\cos(\omega/2)$ is a relevant parameter in determining T_N . However, a quantitative comparison of the derivative $d(\ln T_N)/d(\text{IR})$ and $d\{\ln[\cos^2(\omega/2)]\}/d(\text{IR})$ based on the structural data of Fig. 2 shows that the change due to $\cos^2(\omega/2)$ can account *only* for a small fraction (0.4/9) of T_N . Since an explicit formula of the exchange interaction J as a function of the octahedral-site distortion described by the Q_2 and Q_3 modes has not been worked out, we have to use the

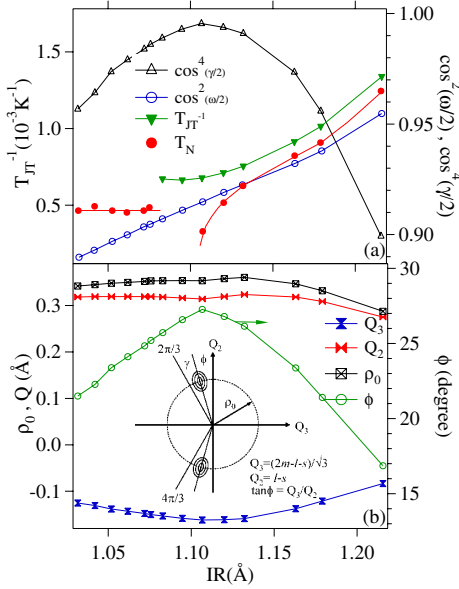


FIG. 3 (color online). (a) The IR dependences of $\cos^2(\omega/2)$, $\cos^4(\gamma/2)$, T_{JT}^{-1} , the angle ϕ , and the octahedral-site distortion modes (Q_2, Q_3) and $\rho_0 = (Q_2^2 + Q_3^2)^{1/2}$. The scale of T_N can be seen in Fig. 1. (b) Inset: The definition of angles ϕ and γ in the (Q_2, Q_3) plane. The schematic contour of the two-well potential is after Ref. [5]. The γ enters the wave functions for the two sites in the crystal structure shown in Fig. 1: occupied at site 1, $\cos(\gamma/2)|3x_1^2 - r_1^2\rangle + \sin(\gamma/2)|y_1^2 - z_1^2\rangle$; unoccupied at site 2: $-\sin(\gamma/2)|3y_2^2 - r_2^2\rangle + \cos(\gamma/2)|x_2^2 - z_2^2\rangle$.

schematic drawing of lattice distortions and orbital occupation in the inset of Fig. 1 to demonstrate how an approximate expression is obtained. We take the same definition of the leaning angle ϕ in the (Q_2, Q_3) plane used by Kanamori [6] and define for clarification a new angle $\gamma = \pi/6 - \phi$ in Fig. 3 to simplify the wave functions. The $\theta_a = 0, 2\pi/3$, and $4\pi/3$ in the (Q_2, Q_3) plane correspond to orbitals $3z^2 - r^2$, $3x^2 - r^2$, and $3y^2 - r^2$, respectively. The wave function is expressed as a linear combination of $3z^2 - r^2$ and $x^2 - y^2$ as θ_a deviates from these angles. Since the two-well potential in $RMnO_3$ is not far from $\theta_a = 2\pi/3$ and $4\pi/3$, calculation of the overlap integral is made much easier by using the angle γ and $(3x^2 - r^2)/(y^2 - z^2)$ and $(3y^2 - r^2)/(x^2 - z^2)$ in the alternate sites in the ab plane [7]. The ferromagnetic superexchange interaction via the virtual charge transfer between the occupied orbital at site 1 and unoccupied orbital at site 2 [see the inset of Fig. 1] brings about a

$$J_{ab}^{\sigma} \sim \cos^4(\gamma/2)\cos^2(\omega/2)|\langle 3x_1^2 - r_1^2 | H' | x_2^2 - z_2^2 \rangle|^2 / \Delta_{\sigma}. \quad (1)$$

The γ dependence in J_{ab}^{σ} makes sense since the orbitals at $\theta_a = 2\pi/3$ and $4\pi/3$ on the alternate sites in the ab plane optimize the overlap integral of the e^0 -O- e^1 interaction. As shown in Fig. 3, $d[\ln \cos^4(\gamma/2)]/d(IR)$ has the wrong sign to account for a reduction of T_N as IR decreases. The angle

ϕ approaches $\pi/6$ from La to Gd, and $GdMnO_3$ has the optimal orbital mixing for e^0 -O- e^1 coupling.

After ruling out the roles of the Mn-O-Mn bond angle and the octahedral-site distortion in determining T_N , we have to consider whether the gap Δ_{σ} of Eq. (1) between the occupied and unoccupied states is the variable determining $T_N(IR)$. With a negligible change of both the $\langle Mn-O \rangle$ bond length and $\langle \theta \rangle$ on crossing T_{JT} [16], which means a small change in the bandwidth according to the formula $b \approx \cos(\omega/2)/d^{3.5}$, $LaMnO_3$ becomes a good conductor and shows a collapsed thermoelectric power at $T > T_{JT}$ [17]. This observation indicates that $LaMnO_3$ is a *Jahn-Teller insulator*, i.e., $\varepsilon_{JT} \approx \Delta \approx 1.6$ eV [18]. However, since the transition at T_{JT} progressively transforms to a semiconductor-semiconductor transition as IR decreases [8], the correlation energy U increases the gap $\Delta = \varepsilon_{JT} + U$ for the $RMnO_3$ perovskites with smaller R^{3+} . In order to determine how the Jahn-Teller splitting ε_{JT} plays a role in the relationship T_N versus IR, the evolution of ε_{JT} versus IR is needed. In the two-well potential of the cooperative JT distortion, the occupied state is located at the bottom of the well near $\theta_a = 2\pi/3$ or $4\pi/3$ in Fig. 3 and the unoccupied state is at the opposite side of the $\rho_0 = (Q_2^2 + Q_3^2)^{1/2}$ circle. Therefore, ε_{JT} is close to the barrier height δE of the three-well potential [19]. But the expression for δE includes a parameter that is not directly measurable. However, from mean-field theory [20,21] $k_B T_{JT} \approx g^2/K$ and from $\rho_0 = g/K$ [19], the electron-phonon coupling constant $g = k_B T_{JT}/\rho_0$ and the phonon stiffness $K = k_B^2 T_{JT}^2/\rho_0^2$ can be obtained from the measurable parameters T_{JT} and ρ_0 in this work, which allows us to further derive $\varepsilon_{JT} = 2g\rho_0$ [22] as $\varepsilon_{JT} \propto k_B T_{JT}$. The octahedral-site distortion described by $\rho_0(IR)$ resembles closely the feature of $T_{JT}(IR)$ in Fig. 1, and the inverse $T_{JT}(IR)$ of Fig. 3 shows a change similar to $T_N(IR)$ in the type-A spin-ordered phase. Moreover, a $d[\ln(1/\varepsilon_{JT})]/d(IR) \approx 7 \text{ \AA}^{-1}$ is remarkably close to the measured $d(\ln T_N)/d(IR) \approx 9 \text{ \AA}^{-1}$. It is clear that the JT distortion in a $MnO_{6/2}$ octahedron perturbs the e -orbital superexchange interaction in the Mn-O_{II}-Mn bonds most efficiently through enlargement of the gap Δ_{σ} .

According to the picture outlined above, the continuous reduction of J_{ab}^{σ} and nearly constant J_{ab}^{π} in $J_{ab} = J_{ab}^{\sigma} - J_{ab}^{\pi}$ as IR decreases could lead to $J_{ab} \approx 0$ while J_c remains unchanged. Neutron diffraction [23] indeed shows a continuous decrease of J_{ab} from 1.67 meV in $LaMnO_3$ to 0.3 meV in $TbMnO_3$ and a more or less constant $J_c \approx -1$ meV for both compounds. The competition between J_{ab}^{σ} and J_{ab}^{π} apparently leads to a suppression of the classic spin ordering in $TbMnO_3$ and $DyMnO_3$. Whereas the next-nearest-neighbor interaction has been invoked [24] to explain the evolution of the magnetic phase of $RMnO_3$ perovskites, the J_{ab}^{σ} vs J_{ab}^{π} competition proposed in this work receives strong support from our structural study. The phase having magnetic-coupling fluctuations due to this competition is unstable relative to the

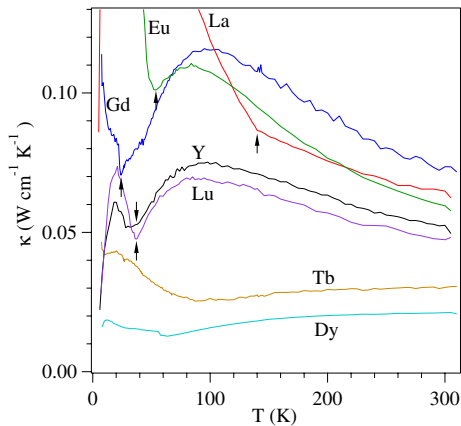


FIG. 4 (color online). Temperature dependence of the thermal conductivity $\kappa(T)$ for the $RMnO_3$ perovskites selected as typical for the three regions: type-A spin order ($R = \text{La, Eu, Gd}$), no classic spin order ($R = \text{Tb, Dy}$), and type-E spin order ($R = \text{Y, Lu}$). Arrows mark the temperature where spins become ordered as detected from the magnetization.

type-E spin order where the Mn-O_{II}-Mn bonds in the ab plane are segregated into J^σ -dominant and J^π -dominant bonds. Ordering of these magnetic interactions in HoMnO_3 gives up-up-down-down spin in a $[110]$ exchange wave while retaining antiferromagnetic coupling along the c axis [25,26]. The mean-field theory [21] gives a $T_N = -8J_{ab} + 4J_c$ for type-A spin ordering. In the phase having type-E spin ordering, however, T_N must be proportional to the magnitude of mean exchange energy, which is segregated into the J^σ -dominant and J^π -dominant bonds that are ordered in the ab plane. Since the balance to either J^σ -dominant or J^π -dominant Mn-O_{II}-Mn bonds depends on the octahedral-site distortion and not on the Mn-O-Mn bond angle, a weak IR dependent ρ_0 in Fig. 3 could explain the IR-independent T_N found in the type-E phase.

Our thermal conductivity $\kappa(T)$ measurements shown in Fig. 4 support this scenario. Figure 4 demonstrates a striking evolution in the paramagnetic phase from a phononlike $\kappa(T)$ in the region where the spins are type-A ordered to a glassy $\kappa(T)$ in TbMnO_3 and DyMnO_3 where spins show no classic ordering and finally back to a phononlike $\kappa(T)$ in the type-E spin-ordered phase. Whether the magnetic-coupling fluctuations in TbMnO_3 and DyMnO_3 are dynamic or static remains to be determined. Nevertheless, it is interesting to note that the magnetic-coupling disorder significantly perturbs the lattice so as to introduce the glassy $\kappa(T)$ to lowest temperatures in the shaded area of Fig. 1.

In conclusion, the IR dependence of the structural and magnetic transitions as well as the local $\text{MnO}_{6/2}$ site distortions for the entire family of $RMnO_3$ perovskites has revealed that the dominant factor determining $T_N(\text{IR})$ in the type-A phase is an increase in the JT splitting ε_{JT} with decreasing IR; the cooperative octahedral-site rotations play only a minor role. Disappearance of T_N in the transitional compounds between those with type-A and type-E

magnetic order occurs at a crossover from positive to negative $J_{ab} = J_\sigma - J_\pi$ where exchange-striction fluctuations suppress $\kappa(T)$; type-E magnetic order is postulated to be an ordered segregation into alternating $J_{ab} > 0$ and $J_{ab} < 0$ Mn-O_{II}-Mn interactions forming an exchange wave propagating along $[110]$.

We thank the Robert A. Welch Foundation and the NSF for financial support. J.-S.Z. is grateful to I. B. Bersuker for helpful discussions.

- [1] J. B. Goodenough, *Phys. Rev.* **100**, 564 (1955).
- [2] Y. Murakami *et al.*, *Phys. Rev. Lett.* **81**, 582 (1998).
- [3] F. Moussa *et al.*, *Phys. Rev. B* **54**, 15 149 (1996).
- [4] M. C. Sanchez, G. Subias, J. Garcia, and J. Blasco, *Phys. Rev. Lett.* **90**, 045503 (2003).
- [5] Z. Popovic and S. Satpathy, *Phys. Rev. Lett.* **84**, 1603 (2000).
- [6] J. Kanamori, *J. Appl. Phys.* **31**, S14 (1960).
- [7] J.-S. Zhou and J. B. Goodenough (unpublished).
- [8] J.-S. Zhou and J. B. Goodenough, *Phys. Rev. B* **68**, 144406 (2003).
- [9] B. Dabrowski, S. Kolesnik, A. Baszczuk, O. Chmaissem, T. Maxwell, and J. Mais, *J. Solid State Chem.* **178**, 629 (2005).
- [10] G. Maris, V. Volotchaev, and T. T. M. Palstra, *New J. Phys.* **6**, 153 (2004).
- [11] J.-S. Zhou *et al.*, *Phys. Rev. B* (to be published).
- [12] J. A. Alonso *et al.*, *Inorg. Chem.* **39**, 917 (2000).
- [13] Y. H. Huang *et al.*, *Chem. Mater.* **18**, 2130 (2006).
- [14] O. Chmaissem *et al.*, *Phys. Rev. B* **64**, 134412 (2001).
- [15] W. A. Harrison, *The Electronic Structure and Properties of Oxides* (Freeman, San Francisco, 1980).
- [16] J. Rodriguez-Carvajal *et al.*, *Phys. Rev. B* **57**, R3189 (1998).
- [17] J.-S. Zhou and J. B. Goodenough, *Phys. Rev. B* **60**, R15002 (1999).
- [18] T. Arima, Y. Tokura, and J. B. Torrance, *Phys. Rev. B* **48**, 17006 (1993).
- [19] I. B. Bersuker, *Electronic Structure and Properties of Transition Metal Compounds* (John Wiley & Sons, New York, 1996), p. 299.
- [20] T. Maitra, P. Thalmeier, and T. Chatterji, *Phys. Rev. B* **69**, 132417 (2004).
- [21] S. Okamoto, S. Ishihara, and S. Maekawa, *Phys. Rev. B* **65**, 144403 (2002).
- [22] D. Feinberg, P. Germain, M. Grilli, and G. Seibold, *Phys. Rev. B* **57**, R5583 (1998).
- [23] R. Kajimoto, H. Mochizuki, H. Yoshizawa, H. Shintani, T. Kimura, and Y. Tokura, *J. Phys. Soc. Jpn.* **74**, 2430 (2005).
- [24] T. Kimura, S. Ishihara, H. Shintani, T. Arima, K. T. Takahashi, K. Ishizaka, and Y. Tokura, *Phys. Rev. B* **68**, 060403 (2003).
- [25] H. W. Brinks, J. Rodriguez-Carvajal, H. Fjellvag, A. Kjekshus, and B. C. Hauback, *Phys. Rev. B* **63**, 094411 (2001).
- [26] A. Munoz, M. T. Casais, J. A. Alonso, M. J. Martinez-Lope, J. L. Martinez, and M. T. Fernandez-Diaz, *Inorg. Chem.* **40**, 1020 (2001).